DNA origami directed nanometer-scale integration of colloidal quantum emitters with silicon photonics

Xin Luo[1, 2], Luigi Ranno[2], Tara Sverko[3], Jae Young Lee[1], Nicholas Sbalbi[2], Annette Jones[3], Chi Chen[1], Moungi G. Bawendi[3], Juejun Hu[2], Robert J. Macfarlane[2]*, Mark Bathe[1]*

Affiliations

[1]Department of Biological Engineering, Massachusetts Institute of Technology, Cambridge, MA, 02139, USA.

[2]Department of Materials Science and Engineering, Massachusetts Institute of Technology, Cambridge, MA, 02139, USA.

[3]Department of Chemistry, Massachusetts Institute of Technology, Cambridge, MA, 02139, USA.

*Corresponding author emails: rmacfarl@mit.edu, mark.bathe@mit.edu

Abstract: Incorporation of colloidal quantum emitters into silicon-based photonic devices would enable major advances in quantum optics. However, deterministic placement of individual sub-10 nm colloidal particles onto micron-sized photonic structures with nanometer-scale precision remains an outstanding challenge. Here, we introduce Cavity-Shape Modulated Origami Placement (CSMOP) that leverages the structural programmability of DNA origami to precisely deposit colloidal nanomaterials within lithographically-defined resist cavities. CSMOP enables clean and accurate patterning of origami templates onto photonic chips with high yields. Soft-silicification-passivation stabilizes deposited origamis, while preserving their binding sites to attach and align colloidal quantum rods (QRs) to control their nanoscale positions and emission polarization. We demonstrate QR integration with photonic device structures including waveguides, micro-ring resonators, and bullseye photonic cavities. CSMOP therefore offers a general platform for the integration of colloidal quantum materials into photonic circuits, with broad potential to empower quantum science and technology.

Main Text

Advances in nanophotonic research and technology, particularly quantum photonic integrated circuits (PICs), demand precise and selective nanoscale spatial control over the fabrication of optically functional materials[1-3]. While conventional top-down fabrication techniques face resolution and scalability limitations[4-8], bottom-up molecular and colloidal synthesis can scalably produce diverse libraries of high-quality optical nanomaterials with nanometer to atomic scale features that possess tunable properties and functions[9-14]. However, a fundamental challenge that limits their utility in photonics circuits persists: colloidal materials are synthesized stochastically in solution but require deterministic, single-particle incorporation into optical and electronic

structures on-chip. For example, precisely organizing single-photon emitting colloidal quantum emitters on PICs could unlock a broad spectrum of applications in quantum sensing, communication and computing[15-18]. However, current methods predominantly rely on inefficient processes such as post-deposition fabrication[19-22] or direct lithography-guided stochastic deposition[23-28], limiting advances in their application. Improved techniques like capillary force-assisted placement are typically limited to large NPs on flat substrates with size-matching traps without programmable selectivity[29-34]. Thus, achieving precise, selective, and scalable integration of colloidal nanomaterials smaller than 10 nm—which is typical of quantum emitters—into topographically complex photonic structures with nanoscale control remains an unsolved challenge.

DNA nanotechnology, particularly DNA origami, has emerged as a scalable bottom-up approach to organize nanoscale optical materials, including molecular emitters[35-37], metallic nanoparticles (NPs)[38-40], upconversion NPs[41], quantum dots (QDs)[42-46] and nanodiamonds[47, 48] into complex hierarchical structures with nanometer-scale accuracy. While typically restricted to solution-based assemblies, the DNA Origami Placement (DOP) method demonstrated positioning of 2D[49-52] and 3D[53] DNA origamis onto landing pads defined by electron beam lithography (EBL), successfully organizing dye molecules[51, 52] and gold nanospheres (AuNSs)[53, 54]. However, quantum emitters such as nanodiamonds and quantum rods (QRs) are unstable in the high ionic strength conditions required for DOP. Furthermore, while alternative lithography methods have been explored for origami placement on various flat substrates[55-60], little progress has been made with practical PIC structures, as their micron-scale topographical features can hinder precise placement and lead to random trapping of colloidal nanomaterials.

Here, we introduce Cavity-Shape Modulated Origami Placement (CSMOP) that enables the precise integration of individual colloidal nanomaterials into photonic devices by leveraging lithographic patterning with DNA origami's ability to control colloidal nanomaterials (**Fig. 1**). Specifically, CSMOP uses EBL to define origami shape-matching cavities in a resist layer, whereby cavity-origami interactions are modulated via topographical confinement, ionic conditions, and origami design to achieve nanometer-scale spatial position and orientation. Deposited origamis are designed with hybridization overhangs that enable subsequent capture of DNA-functionalized nanomaterials. Using this platform, we demonstrate high-yield AuNS arrays and orientation-controlled gold nanorods (AuNRs) for anisotropic light scattering. Additionally, we establish a soft-silicification-passivation strategy that stabilizes CSMOP origami attachment while preserving the overhang hybridization capability to assemble and orient QRs in lower ionic strength conditions required for their colloidal stability. These QR arrays exhibit controlled emission polarization and minimal background emission after resist lift-off. We demonstrate deterministic placement of individual QRs on silicon nitride (SiN_x) waveguides, micro-ring resonators, and bullseye cavities. Thus, CSMOP provides a general platform for precise incorporation of colloidal quantum emitters into PICs, offering valuable new opportunities for quantum photonics[61-63].

Cavity-shape modulated origami placement

CSMOP uses topographical cavities in the resist layer to modulate DNA origami placement and subsequent nanomaterial integration, providing two key advantages over the previous approach[51,

[52]. First, the resist layer prevents random attachment of nanomaterials to the background by acting as a physical barrier, and removes unintentional accumulation of materials through resist lift-off. Second, shape-matching confinement regulates origami orientation and minimizes aggregation[34, 49, 64, 65]. We fabricated origami-shape matching cavities within a poly(methyl methacrylate) (PMMA) resist layer using a standard EBL process (see **Methods** and **Supplementary Fig. 1**). We employed 2D six-helix bundle (6HB) wireframe origamis (**Supplementary Fig. 2** and **Supplementary Note 1**) as the model platform for CSMOP to leverage their planarity and rigidity[66, 67]. One side of the origami was functionalized with single-stranded DNA (ssDNA) overhangs of two sequences: the NP binding sequence (**Fig. 1a**, red) and 20-nucleotide polythymidine (**Fig. 1a**, green), with the latter acting as entropic brushes to prevent binding of the functionalized origami face to the substrate[43, 52] and ensure the access to the binding overhangs.

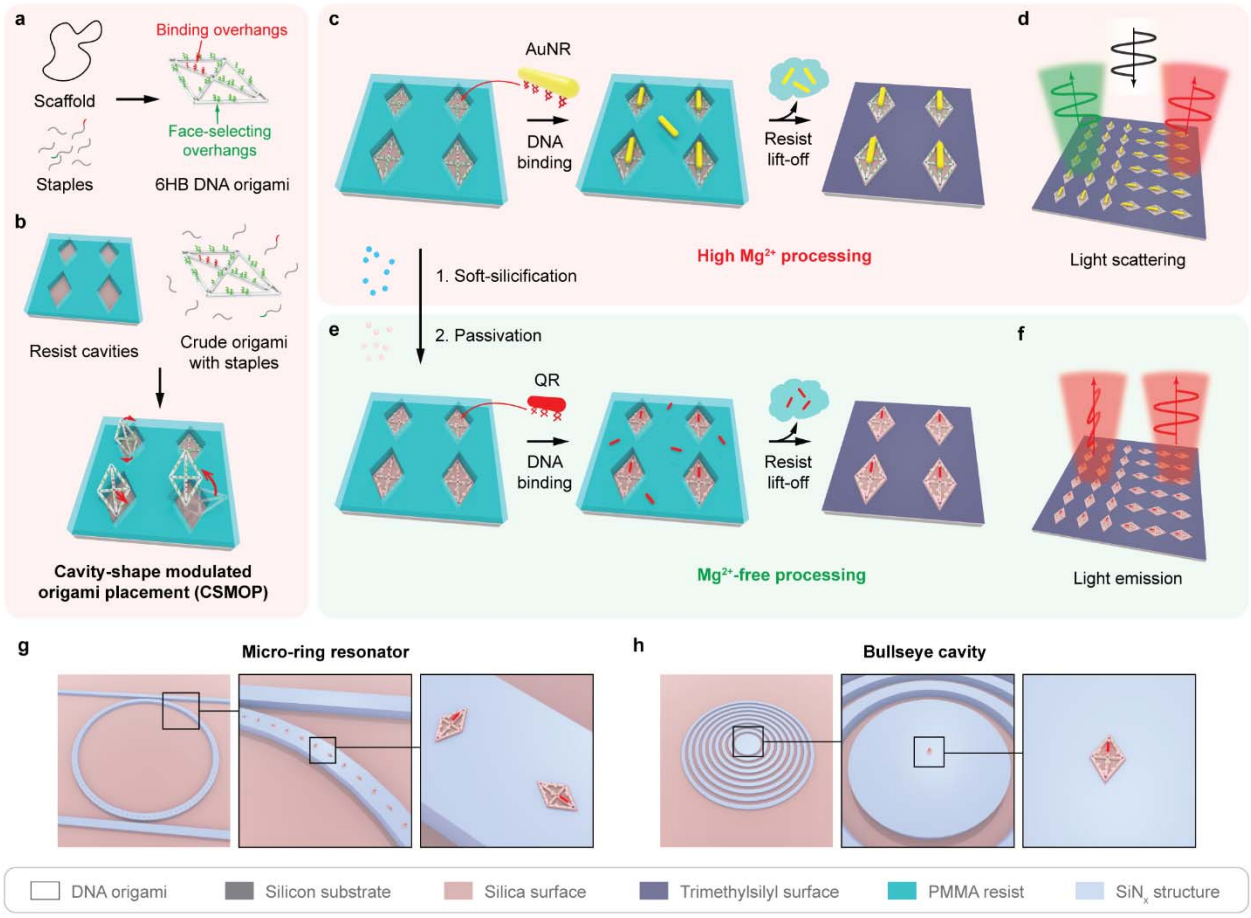

Fig. 1. Overview of CSMOP and its application to deterministic nanoscale placement of AuNRs and QRs. a, Design and assembly of planar DNA origami. **b**, Cavity-shape modulated placement of origamis with binding overhangs facing up at the base of EBL-defined cavities in the PMMA resist layer. **c**, AuNR attachment and alignment to CSMOP-directed origami under high Mg^{2+} concentration. **d**, Illustration of a CSMOP-directed AuNR array with controlled plasmonic light scattering. **e**, Soft-silicification and passivation of origami within the cavity to attach and align QRs under Mg^{2+}-free conditions. **f**, Illustration of a CSMOP-directed QR array with controlled light emission polarization. **g–h**, CSMOP-enabled deterministic incorporation of individual QRs into micro-ring

resonators (g) and bullseye photonic cavities (h) with positional and orientational control. Surface chemical modifications are omitted in **g** and **h** for clarity.

We first performed CSMOP with 35 mM $MgCl_2$ using a rhombic 6HB wireframe origami with diagonal axes of approximately 75 nm and 125 nm. Notably, the CSMOP method proved effective using crude, unpurified origami in solution, eliminating the need for origami purification following self-assembly, which not only streamlined the workflow but also avoided material loss and origami aggregation associated with purification processes[68, 69]. In a typical CSMOP process, a crude rhombic origami solution was applied to a chip bearing EBL-fabricated rhombic-shaped cavity arrays (**Fig. 2a**, left; **Supplementary Fig. 3**), incubated at 23 °C for 2 h, and washed to remove excess DNA (see **Methods**). Atomic force microscopy (AFM) confirmed origamis positioning at cavity bases (**Fig. 2a**, middle; **Supplementary Fig. 4**), while subsequent PMMA lift-off removed the resist layer and any background residuals to produce clean origami arrays on the substrate (**Fig. 2a**, right; **Supplementary Fig. 5**). Origami silicification prior to lift-off rendered the origami structures robust and visible under scanning electron microscopy (SEM) (see **Methods**). We fabricated a 5.5 µm × 5 µm silicified CSMOP array, comprising six strips of rhombic origamis with various orientations and spacings (**Fig. 2b**, **Supplementary Figs. 6–7**). No background contamination was observed across the array after lift-off, further highlighting the cleanliness and scalability of CSMOP.

To demonstrate the versatility, we successfully applied CSMOP to a ladder-shaped 6HB wireframe origami and a single-layer triangular origami, producing large scale arrays of high yields (**Supplementary Figs. 8–12**). Moreover, it is worth noting that CSMOP workflow was developed with straightforward and scalable setups and operations compared to existing methods, demonstrating potential for seamless integration into standard foundry fabrication processes (see **Supplementary Fig. 13** and **Supplementary Note 2** for detailed discussion).

To better understand how topographical confinement regulates origami placement, rhombic-shaped cavities of increasing sizes (size 1 to 3, see **Methods**) were prepared (**Supplementary Fig. 3**). Post-CSMOP analysis revealed that as cavity size increased from size 1 to 2 and 3, the yield of correctly placed DNA origami monomers decreased from 85% to 61% and 11% (N = 288 each), while the occurrence of multiple origamis positioned within the same cavity rose from 3% to 27% and 86%, respectively (**Fig. 2c**, **Supplementary Fig. 14**). This trend indicated relatively strong origami-substrate interactions under 35 mM Mg^{2+}. To modulate origami binding kinetics, we added 100 mM Na^+ to the DNA origami placement solution expecting weakened Mg^{2+}-bridged interactions between origamis and the substrate[43, 70-72]. This significantly reduced the occurrences of multiple DNA origami binding and increased monomer placement yields to 90%, 91%, and 88% for cavity sizes 1, 2, and 3, respectively (N = 576 each) (**Supplementary Fig. 5**). Incorporating silicification prior to removal of the PMMA resist further improved placement yield to 97% (N = 576, size 3) (**Fig. 2c**, **Supplementary Fig. 15**).

To understand the cavity confinement mechanism, we performed thermodynamic binding energy calculations and kinetic simulations (see **Methods** and **Supplementary Note 3**). Without cavities, simulations revealed numerous local energy minimum states away from the correct conformation (**Fig. 2d**, **Supplementary Figs. 16–17**), with only ~0.46 probability of correct placement. By contrast, CSMOP simulations showed a single aligned conformation (P = 1.00), as topographical confinement eliminated local energy minima (**Fig. 2e**). The simulations also suggested that origami rigidity is important to reduce kinetically trapped conformations with

CSMOP (**Supplementary Note 4**). Same effects were observed in simulations of ladder-shaped and triangular origamis (**Supplementary Figs. 19–20**). Thus, rigid origami orientation could be controlled precisely with cavity confinement. We defined rhombic origami orientation as the angle of its long-diagonal-axis, between −90° and +90°. Using a horizontal rhombic cavity array, 81% of origami monomers oriented horizontally within 0 ± 5° following CSMOP (standard deviation: 4°, N = 245) (**Fig. 2f**, grey; **Supplementary Fig. 14a**). In contrast, an array with alternating +45° and −45° rhombic cavities resulted in 86% of origamis oriented within +45° ± 5° or −45° ± 5° (standard deviations: 4° and 3°, respectively, N = 236) (**Fig. 2f**, green; **Supplementary Fig. 21**). CSMOP therefore provides a robust foundation to position and orient colloidal optical materials for photonic devices.

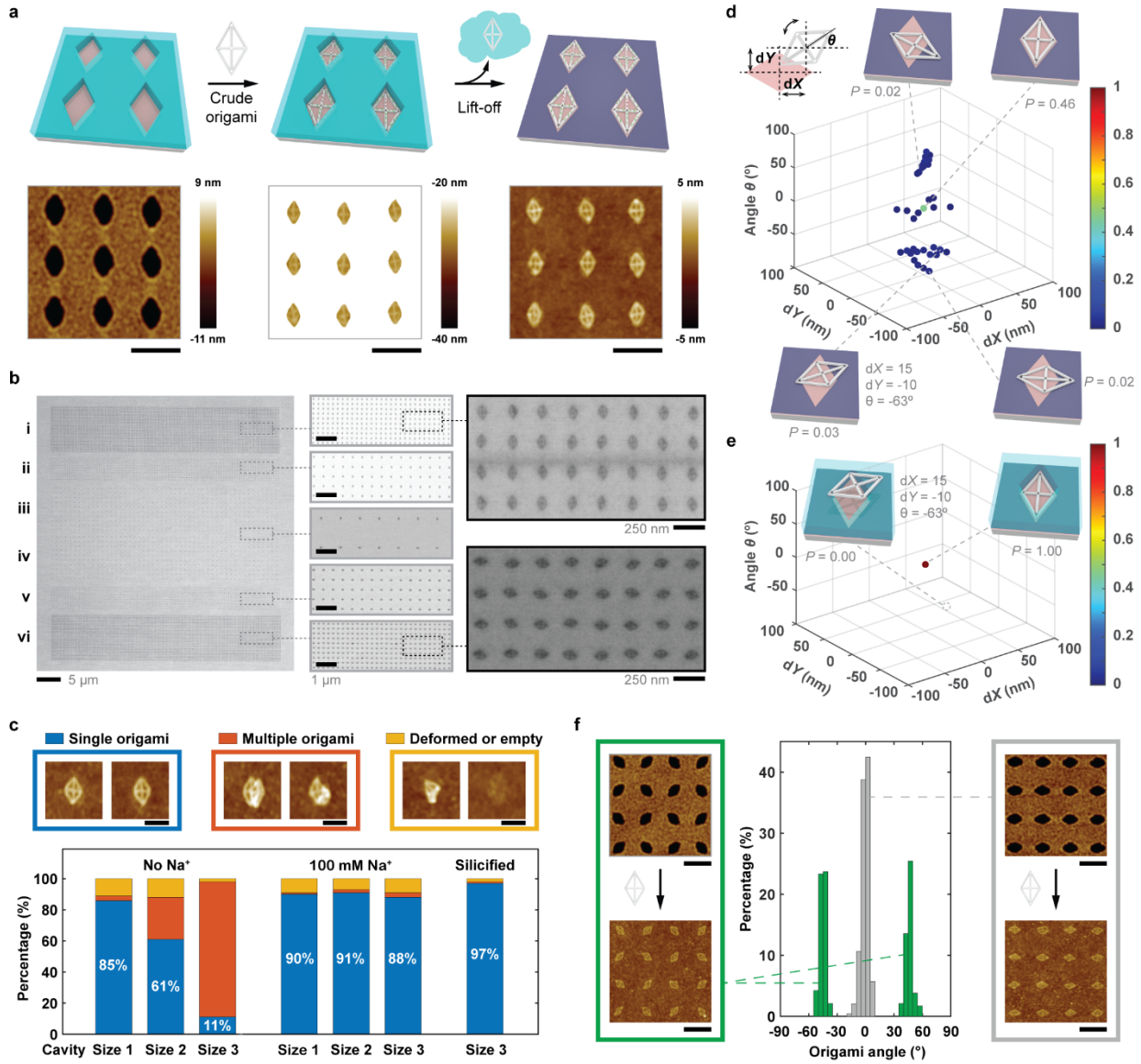

Fig. 2. Cavity-shape modulated placement of 6HB wireframe origami. a, Illustrations (top) and AFM images (bottom) of the CSMOP process applied to a rhombic 6HB wireframe origami. Left: rhombic-shaped cavity; middle: rhombic origami placed at the base of the cavity; Right: origami array after resist lift-off. **b**, SEM images of a silicified CSMOP array with rhombic origamis oriented vertically (i, ii, iii) and horizontally (iv, v, vi) and spaced 250 nm (i, vi), 500 nm (ii, v) or 1 μm (iii, iv) apart. **c**, Statistics of CSMOP-directed rhombic origami using

increasing cavity sizes (size 1 to 3, see **Methods**) with no Na^+ (left), 100 mM Na^+ (middle), or 100 mM Na^+ and silicification (right). Inset: representative AFM images of correctly placed single origamis (blue), multiple origamis in one cavity (orange), and deformed origamis or empty cavities (yellow). **d** and **e**, Kinetic simulation prediction of probabilities (P) of origami conformations (dX, dY, θ) from origami placement without (d) or with (e) cavities. Insets show schematic illustrations of origami conformations of corresponding data points. **f**, Rhombic origami orientational distribution and AFM images from CSMOP using a cavity array of 0° (right, grey), and a cavity array of +45° or −45° (left, green) cavity orientations. AFM scale bars: 250 nm for **a**, **f**; 100 nm for **c**.

CSMOP-directed gold NP arrangement

While single-particle arrangement of metallic NPs, including gold, has been achieved through lithography-guided placement[34, 65, 73], DNA origami offers unparalleled capabilities to position different NPs at pre-determined sites on an origami breadboard with an uncertainty margin down to 1.2 nm[39], facilitating precisely engineered functionalities[38-40]. Previous attempts at deterministic origami-directed gold NP arrangement on chips have been limited to AuNSs using the DOP method on flat surfaces, which can suffer from aggregation and non-specific adsorption[53, 54, 74]. We demonstrate the capability of CSMOP to direct the clean placement of both colloidal AuNSs and AuNRs on EBL-patterned arrays.

We designed and assembled ladder-shaped 6HB wireframe origami with either one (**Fig. 3a**, bottom left) or two (**Fig. 3b**, top) binding sites expressing overhang sequences complementary to DNA strands functionalized to AuNSs. After origami placement and incubation with the AuNS solution, AFM revealed primarily single or paired AuNSs at cavity bases templated by origamis with one or two binding sites, respectively (**Fig. 3a**; **Supplementary Figs. 22–23**). While random AuNS depositions were observed on the resist background (**Supplementary Figs. 22–23**), subsequent resist lift-off removed them, leaving clean arrays of origami-directed single AuNSs or AuNS dimers (**Fig. 3a–b**; **Supplementary Figs. 24–25**). We achieved 86% placement yield for single AuNSs and 75% for AuNS dimers (N = 432 each, **Fig. 3c**), surpassing previously reported yields[54].

The ability to arrange DNA binding overhangs on origami into customized geometries enables CSMOP to both position and orient anisotropic optical nanomaterials. For example, AuNRs have emerged as versatile plasmonic structures for nanophotonics due to their strong, tunable, anisotropic plasmonic properties[75]. Here we demonstrated CSMOP-directed arrangement of AuNRs (75 nm × 18 nm) into arrays with orthogonal orientations using rhombic origamis with five binding overhangs arranged along the long axis (**Fig. 3d**). AFM imaging confirmed AuNRs assembled on the rhombic origami both before and after lift-off, with an individual AuNR placement yield of 68% (N = 800) (**Fig. 3e**; **Supplementary Figs. 26–27**). Deviation from ideal AuNR alignment is attributed to capillary force-driven reconfiguration during the drying process (**Supplementary Fig. 28** and **Supplementary Note 5**).

Because plasmonic light scattering of AuNRs depends on both wavelength and polarization angle, CSMOP can prepare substrates with anisotropic light scattering by aligning arrays of AuNRs in different orientations[76-78] (**Fig. 3f**). We fabricated a 5 µm × 4.5 µm AuNR array comprising four strips containing rhombic origamis oriented vertically or horizontally (**Fig. 3g**; **Supplementary Figs. 27, 29**). Under unpolarized incident light, vertically aligned AuNRs (i and ii) primarily scattered red light along the vertical direction (analyzer direction) arising from longitudinal plasmon resonance, while horizontally aligned AuNRs scattered primarily green

light from transverse plasmon resonance (**Fig. 3g**). Under polarized incident light (without an analyzer), AuNR arrays appeared as red, green, or a mixture depending on their orientation relative to the polarization of the incident light (**Fig. 3h**). Using this method, we created a pattern of the MIT logo with dynamic tunable coloration (**Supplementary Fig. 30**). The ability of CSMOP to exploit anisotropic plasmonic properties of AuNRs shows promising potential for applications in metasurfaces[79, 80] and optical data storage[81, 82].

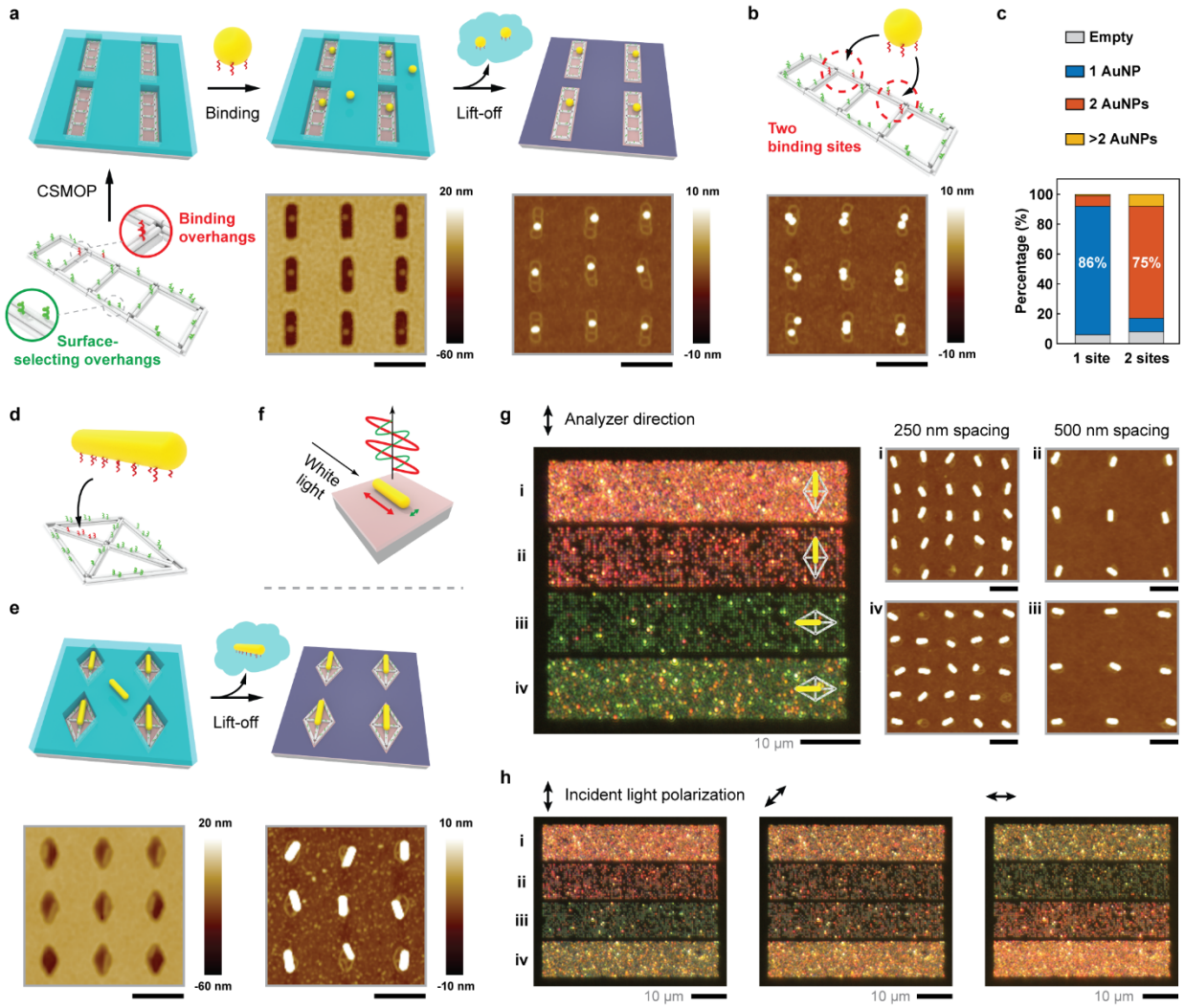

Fig. 3. CSMOP-directed AuNS and AuNR arrays. a, Illustrations and AFM images of CSMOP-directed AuNS arrangement templated by ladder-shaped origami bearing 1 binding site (3 overhangs). AFM images show organized AuNSs within cavities (middle) and after lift-off (right). **b**, CSMOP-directed arrangement of AuNS dimers with 2 binding sites on origami. **c**, Statistics of AuNS monomers and dimers arranged through CSMOP with origamis bearing one or two binding sites. **d**, Illustration of linearly arranged binding overhangs on rhombic origamis for the binding and alignment of AuNRs. **e**, Illustration and AFM images of CSMOP-directed AuNR arrangement within the cavity (left) and after lift-off (right). **f**, Illustration of polarization- and wavelength-dependent light scattering from AuNR arrays. **g**, Dark-field microscopy image of CSMOP-directed AuNR arrays with vertical (i, ii) or horizontal (iii, iv) orientations and 500 nm (i, iv) or 250 nm (ii, iii) AuNR spacings. Scattered light was observed through a vertically-aligned analyzer using unpolarized incident light. **h**, Dark-field microscopy images of the AuNR

array with incident light polarized vertically (left), diagonally (45°, middle) and horizontally (right) without an analyzer. All AFM scale bars: 250 nm.

CSMOP-directed QR arrangement

Colloidal quantum emitters like QDs and QRs have well-engineered scalable syntheses and tunable optical and electronic properties, making them attractive for electronics[83], light-emitting devices[84] and quantum information science[85]. QRs, in particular, offer unique opportunities to engineer efficient coupling with photonic devices owing to their morphology-dependent emission polarization[86-89]. However, DNA-functionalized QRs typically aggregate under high Mg^{2+} concentrations required for origami placement. While previous research showed origami-substrate attachment under Mg^{2+}-free environments using carefully designed crosslinking reactions[50], DNA hybridization accessibility after such reactions remains undemonstrated. Here, we introduce a straightforward and versatile soft-silicification-passivation method to enhance the attachment of CSMOP origamis under Mg^{2+}-free conditions, enabling the arrangement of metastable colloidal quantum emitters like QRs (**Fig. 4a**).

Specifically, we carefully silicified CSMOP-directed origamis within cavities to secure origami attachment while preserving the accessibility of NP binding overhangs (see **Methods**). AFM imaging revealed that origami height remained stable around 2.6 nm after up to 1.5 h of silicification, then increased to 5.3 ± 0.4 nm over 72 h (**Supplementary Fig. 31**), indicating silica deposition. We found that as short as a 1.5-hour silicification could ensure stable origami attachment under Mg^{2}□-free conditions (termed soft-silicification, compared to days of silicification in previous work[53, 90-92]). However, direct QR incubation with silicified origami resulted in random QR attachment, likely due to non-specific electrostatic attractions to positively charged silica surfaces (**Supplementary Fig. 32**). We addressed this by passivating the silica surfaces with negatively charged silane, promoting QR binding exclusively through DNA hybridization (**Fig. 4b**). This yielded individual QRs at each CSMOP origami position with 79% single QR placement yield (N = 720) (**Supplementary Figs. 33–34**). Orientational analysis showed 73% single QRs oriented within 90 ± 30° with vertical CSMOP template (N = 346) (**Fig. 4c**, green; **Supplementary Fig. 33**), and 67% exhibited 0 ± 30° orientation with horizontal CSMOP (N = 326) (**Fig. 4c**, orange; **Supplementary Fig. 34**). Notably, we observed clusters of QR orientations deviating by around ±30° from the designed orientation (**Fig. 4c**, arrows), which can be attributable to capillary force-driven reconfigurations within origamis (**Supplementary Fig. 35**). While ssDNA hybridization to silicified origami has been reported[92], we demonstrate attachment of DNA-functionalized NPs through soft-silicification-passivation, overcoming additional challenges of aggregation and steric hindrance.

Using this protocol, we fabricated QR arrays with controlled position and alignment. Widefield fluorescence microscopy revealed photoluminescence (PL) emission from individual QRs under 532 nm excitation (**Fig. 4d**), with stochastic intermittency (*i.e.*, blinking) and non-radiative populations (**Supplementary Video 1**). QD blinking and non-radiative states are ubiquitous phenomena associated with surface traps and charging-induced Auger recombination[93, 94], which can be mitigated through QD surface passivation[95, 96] or external optical manipulation[97]. To demonstrate deterministic emission polarization control, we monitored PL intensity versus analyzer angle from two QR arrays with orthogonal orientations (**Supplementary Fig. 36**). Results showed sinusoidal relationships with roughly anti-correlated PL intensities (**Fig. 4e**), indicating ensemble alignment of QRs in respective arrays with roughly

orthogonal orientations. The offset between the maximum and the minimum of the two QR array intensities, respectively, was attributed primarily to the sizeable QR orientation outliers around ± 30°. Notwithstanding, this represents the first demonstration of controlling polarized emissions from individual colloidal emitters through deterministic engineering of emitter configurations on device substrates.

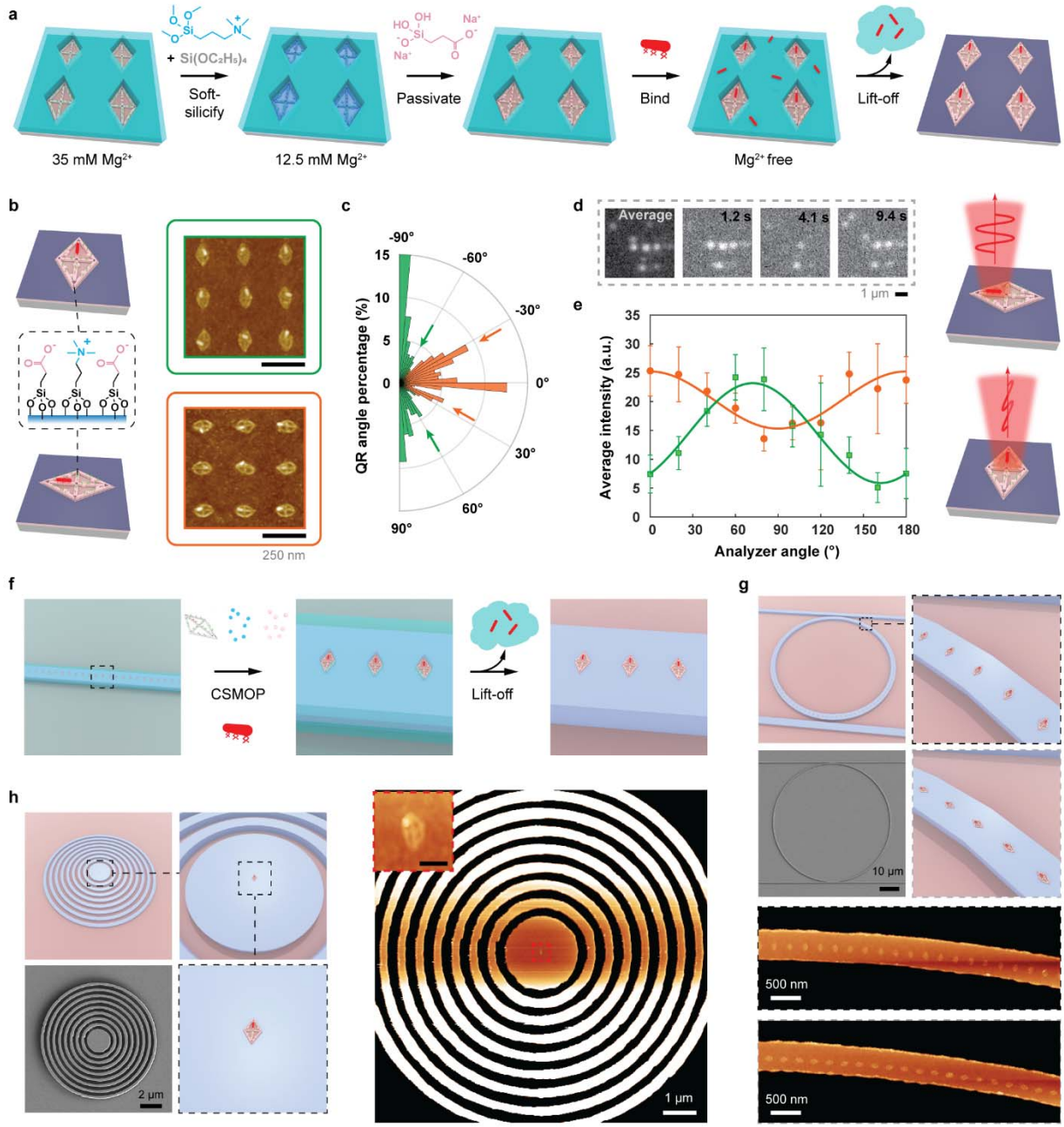

Fig. 4. CSMOP-directed QR arrangement. a, Schematic illustration of the workflow: CSMOP array soft-silicification, passivation, QR binding, and lift-off. **b**, Illustration of origami surface charge after soft-silicification-passivation (left) and AFM images of CSMOP-directed individual QR binding to vertically (top right, green) and horizontally (bottom right, orange) aligned origamis. **c**, Orientation distribution of QRs directed by vertical (green) and horizontal (orange) CSMOP origamis. Arrows highlight major orientation deviations from design. **d**, Widefield PL images of a CSMOP directed QR array at different time points. The average image is a maxima-projection of 100

frames over 10 s. Frame exposure time: 100 ms. **e**, Averaged PL intensity as a function of the analyzer angle from vertically (green) and horizontally (orange) aligned QR arrays. **f**, Schematic illustration of CSMOP-directed QR placement on SiN_x waveguide with an orthogonal orientation. Trimethoxysilyl coatings are omitted for clarity. **g**, Illustration and AFM images of CSMOP-directed QRs on a micro-ring resonator with orthogonal (black box) or parallel (grey box) orientations. The SEM image shows the micro-ring structure. **h**, Illustration and AFM images of a single CSMOP-directed QR at the center of a bullseye cavity. The SEM image shows the bullseye cavity structure.

CSMOP-directed deterministic QR integration with silicon photonics

Integrating colloidal quantum emitters within practical devices typically requires their placement on non-uniform topographies[15-18]. CSMOP provides important advancement in this regard, as the cavity resist layer prevents non-specific adsorption to structures. To demonstrate deterministic integration of individual colloidal quantum emitters within silicon photonics, we fabricated chips with 310 nm high SiN_x photonic structures on silicon, including waveguides, micro-ring resonators, and bullseye cavities (**Supplementary Fig. 37**). We first evaluated CSMOP on slab waveguides, a fundamental building block of PICs (**Fig. 4f**). Specifically, SiN_x structures were treated with O_2 plasma to create surface silanol groups. After PMMA coating, cavities orthogonal or parallel to the waveguide were fabricated on the slab surface using EBL, with cavity depths of 46 nm, 62 nm, or 86 nm for waveguides of 0.5 µm, 1 µm, and 2 µm width, respectively, due to topography-affected resist coating (**Supplementary Fig. 38**). After CSMOP, we observed a high origami placement yield of 94% (N = 336) on 2 µm SiN_x slab waveguides, despite a deeper cavity depth (86 nm) than that on a flat substrate (~30 nm) (**Supplementary Fig. 39**). Subsequent QR attachment created deterministically placed individual QRs on SiN_x waveguides with a 43% (N = 329) placement yield (**Supplementary Fig. 40**). We also demonstrated deterministic CSMOP-directed QR placement on SiN_x micro-ring structures with potential applications in lasers[98] and optical sensors[99] (**Fig. 4g**; **Supplementary Fig. 41**). QR orientation was engineered to be perpendicular or parallel to the tangential direction of the ring.

Bullseye cavities are promising photonic structures for quantum optics[100], but a key challenge is positioning the emitter at the cavity center to avoid artificial defects, such as uncontrolled emission polarization[101]. We harnessed the capability of CSMOP to deterministically place a single QR at the center of a bullseye cavity (**Fig. 4h**; **Supplementary Fig. 42**), achieving a yield of 49% (18 out of 37 bullseye structures imaged). With tailored photonic structure materials and colloidal quantum emitters, this would enable scalable fabrication of single-photon sources for potential quantum PICs (**Supplementary Note 6**). Importantly, we note that DNA origami placement is compatible with various optical device materials, including diamond-like carbon[49], glass[60], TiO_2[102], and semiconductor 2D materials like graphene[103, 104] and transition metal dichalcogenides[105]. This versatility extends the breadth of potential applications of CSMOP well beyond silicon-based photonics[3, 106].

Conclusions

The CSMOP method effectively bridges bottom-up molecular and colloidal synthesis with top-down fabrication of practical photonic devices. Combining DNA origami with EBL-defined cavities, we achieved precise integration of nanoscale optical materials with photonic circuit structures. CSMOP demonstrated successful arrangement of AuNS arrays and controlled

orientation of anisotropic AuNRs, advancing numerous possibilities for nanoplasmonics. Our soft-silicification-passivation strategy exhibited stable origami attachment to device substrate while maintaining DNA hybridization capabilities, overcoming challenges in integrating metastable colloidal QRs. This enabled deterministic positioning of individual quantum emitters within complex photonic architectures, including waveguides, micro-ring resonators, and bullseye cavities. CSMOP's built-in lift-off process ensures clean device surfaces with minimal background, while its compatibility with standard nanofabrication processes offers promising potential for practical applications. CSMOP offers several important advantages over conventional nanofabrication techniques, providing nanometer-scale control, scalable bottom-up fabrication, and broad compatibility across various nanomaterials. Ultimately, CSMOP provides a universal platform for the precise integration of diverse colloidal nanomaterials with functional solid-state devices, establishing the foundation for next-generation technologies spanning quantum photonics, nanoelectronics, biosensing, and advanced materials engineering.

Methods

DNA origami design and assembly

6HB wireframe origamis were designed using ATHENA[107]. Design details and DNA sequences are provided in **Supplementary Note 1**. Origamis were folded in a 12.5 mM $MgCl_2$ buffer containing 40 mM Tris (tris(hydroxymethyl)aminomethane) and 12.5 mM $MgCl_2$ (pH = 8.0 ± 0.2)[108]. Specifically, 2 nM DNA scaffold (M13mp18/p7249, Tilibit nanosystems) was mixed with 20 equivalent unmodified staple strands and 60 equivalent modified staple strands (standard desalting, Integrated DNA Technologies (IDT)) in 12.5 mM $MgCl_2$ buffer. The mixed solution was annealed in a thermocycler (Biorad T100) using the following program: 95 °C for 5 min, 85 °C to 76 °C at 5 min/°C, 75 °C to 30 °C at 13.75 min / 0.5 °C, 29 °C to 25 °C at 10 min/°C, then held at room temperature (*ca.* 23 °C). The folded origami sample was used directly for CSMOP without further purification.

DNA functionalization of NPs

All NPs were functionalized with a thiolated ssDNA purchased from IDT with standard desalting (sequence: /5ThioMC6-D/TTTTTTTTTCCCAGGTTCTCT) as a disulfide-modified strand and further reduced by 100 equivalent Tris(2-carboxyethyl)phosphine hydrochloride (TCEP) at a final concentration of 1 mM.

AuNSs were functionalized using a freezing-assisted method[109]. Citrate-stabilized AuNS (17 nm diameter) was synthesized following a standard seeded growth protocol[110]. 1 mL crude AuNS (~2 nM) was mixed with 6000 equivalent thiolated DNA and kept in a −80 °C freezer for 15 min, followed by defrosting at room temperature. Thawed AuNS solution was washed six times with 10 mM NaCl buffer (10 mM Tris, 10 mM NaCl, pH = 8.0 ± 0.2) by centrifugation at 16000 rcf for 3 min and quantified by UV-vis absorption at 450 nm (extinction coefficient: 324000000 $M^{-1}cm^{-1}$).

AuNRs were functionalized using a dehydration-assisted method[111]. 2 mL 0.1 nM citrate-stabilized AuNR (nanoComposix, catalog number: GRCN800) was pelleted by centrifugation at 6000 rcf for 5min and mixed with 30000 equivalent thiolated DNA, with a final volume of around 20 µL. 180 µL 1-butanol was added to the mixture, followed by brief vortex mixing. 200

µL 10 mM NaCl buffer was then added followed by another quick vortex mixing and brief centrifugation to facilitate liquid phase separation, with DNA-functionalized AuNRs dispersed in the bottom aqueous phase. The AuNR solution was collected and washed six times with 10 mM NaCl buffer by centrifugation at 4000 rcf for 4 min and quantified by UV-vis absorption at 830 nm (extinction coefficient: 5900000000 $M^{-1}cm^{-1}$).

QRs was functionalized using a ultrasonication-dehydration-assisted method[43]. 10 µL 5 mg/mL CdSe/CdS core-shell type QRs in hexane (Sigma, catalog number: 900514) was mixed with 500 equivalent thiolated ssDNA in the presence of 100 mM NaOH for a final volume around 50 µL. The mixture was ultrasonicated at 37 kHz for 5 min, immediately followed by adding 600 µL 1-butanol and brief vortex mixing. 200 µL 10 mM NaCl buffer was then added to the mixture followed by another quick vortex and brief centrifugation to facilitate liquid phase separation, with DNA-functionalized QRs dispersed in the bottom aqueous phase. The QR solution was collected and washed using an ultracentrifugal filter (Amicon 100 kDa) six times (8000 rcf 3 min) and quantified by UV-vis absorption at 350 nm (extinction coefficient: 64850000 $M^{-1}cm^{-1}$).

SiN_x photonic structure chip fabrication

The fabrication started with a 100 mm Si (100) wafer (p-type Boron-doped) with 3 µm thermally grown wet oxide (prime grade, University Wafer Inc.). Upon receipt, the wafer was thoroughly cleaned following the RCA clean protocol. RCA-1 (7:2:2 mixture of DI water : ammonium hydroxide : hydrogen peroxide) followed by RCA-2 (7:2:2 mixture of DI water : hydrochloric acid : hydrogen peroxide). For each step, the solution was heated to 75 °C and the wafer was cleaned for 10 min, followed by DI water rinse. After the complete RCA clean, the wafer was dried using a spin rinse dryer. Then, the wafers were loaded in a Low-Pressure Chemical Vapor Deposition Chamber (Tystar Mini Tytan 4600) to deposit the SiN_x layer. at 770 °C, with a pressure of 250 mTorr, 25 sccm of dichlorosilane and 75 sccm of ammonia, resulting in a growth rate of *ca.* 3.41 nm/min. A thickness of 310 nm was targeted for the SiN_x film. After growth, the refractive index and thickness were characterized with reflectometry (Filmetrics F50) and ellipsometry (J.A. Woolam model RC2), followed by singulation of the wafer into individual pieces through cleaving.

For waveguide patterning, chips were first coated with hexamethyldisilazane (HMDS) at 150 °C in a YES-310TA vapor prime oven for 1 min (Yield Engineering Systems Inc). A thin UV-sensitive negative photoresist (AZ-nLOF 2020, Microchemicals GmbH) was coated using a CEE Apogee Spin coater at 2000 rpm for 60 s, followed by baking at 110 °C for 1 min. Before spinning, the photoresist was first diluted in an equal amount by volume of methyl isobutyl ketone to achieve a lower thickness, more suitable for high lithographic resolution. The chips were subsequently coated with a thin conductive layer (ESpacer 300Z from Resonac) by spin coating at 4000 rpm for 45 s. Exposure was performed using an ELS-BODEN EBL system (Elionix HS-50), with 10 nA current and 50 keV beam voltage. After exposure, chips were rinsed in water to remove the conductive layer, post exposure baked at 115 °C for 1 min, developed in a 2.38% TMAH-based developer (AZ 726) for 2 min, and thoroughly rinsed with deionized water. The patterned chips were dry etched using an Inductively Coupled Plasma Reactive Ion Etcher (Samco RIE-230iP) at 1 Pa pressure, 300 W ICP power, 100 W bias power, 20 sccm of CF_4 and 60 sccm of Ar. After etching, the photoresist mask was stripped using an O_2 plasma (ESI 3511V-001).

Fabrication of resist cavity on silicon chips

Resist layer cavities were fabricated via standard EBL. Silicon chips (1 cm × 1 cm) cleaved from a 100 mm Si (100) wafer (p-type Boron-doped) with 90 nm dry thermal oxide (prime grade, University Wafer Inc.) were first cleaned by ultrasonication in isopropanol (IPA) for 10 min and dried with pressurized N_2, followed by O_2 plasma treatment at 500 W, 255 duty ratio with 10 sccm O_2 for 2 min on a Tergeo Plus Plasma Cleaner (PIE Scientific LLC). After priming with HMDS at 150 °C in a YES-310TA vapor prime oven (Yield Engineering Systems Inc) for 1 min, PMMA resist (950 A2 in anisole, MicroChem) was spin coated at 4500 rpm for 1 min and baked at 180 °C for 5 min, yielding around 60 nm thick resist layers. Next, EBL exposure was performed with various doses using an Elionix HS-50 with 2nA operating current and 50 keV beam voltage. The target cavity dimensions were 150 nm × 80 nm (long and short axes length) for the rhombic structure, 150 nm × 40 nm (length and width) for the ladder-shaped structure, and 145 nm (edge length) for the equilateral triangular structure. Proximity effect correction was applied for 250 nm spacing cavities with the BEAMER software. Patterns were developed with MIBK/IPA 1:3 (MicroChem) at 4 °C for 50 s, rinsed with IPA, dried with pressurized N_2, and then exposed to directional O_2 plasma on a RIE-230iPC system (SAMCO) for 18 s at 20 °C, 2.7 Pa with 50 W bias and 20 sccm O_2. Post-RIE was measured to be around 30 nm. Increasing EBL doses from 1020 μC/cm^2 to 1320 μC/cm^2 and 1722 μC/cm^2 resulted in 97 × 135 nm (size 1), 106 × 150 nm (size 2), and 114 × 161 nm (size 3) as the short and long axes length of the rhombic cavity openings measured by AFM (N = 144 each), respectively. Note that AFM measurements were convoluted with probe size and imaging parameters, and O_2 plasma etching expanded the cavity opening, both with potential bias on sharp cavity vertices.

For typical experiments, identical patterns were fabricated on both halves of each chip, which were then cleaved into two 0.5 cm × 1 cm pieces using a PELCO LatticeAx 420 system (Ted Pella Inc). For SiN_x photonic structure chips (1 cm × 1 cm), the process remained unchanged except that 950 PMMA A4 was employed, followed by spin coating of DisCharge H_2O (4×, DisChem Inc) to improve electron conductivity. After aligned EBL exposure with global fiducial markers, the chips were first rinsed with water to remove the DisCharge coating, then developed using the same setup for 90 s.

Cavity modulated origami placement

Crude DNA origami directly from folding at 2 nM in 12.5 mM $MgCl_2$ buffer was adjusted to 1 nM with a final $MgCl_2$ concentration of 35 mM and NaCl concentration of 100 mM. 20 μL crude origami solution was pipetted onto a 0.5 cm × 1 cm silicon chip bearing EBL-fabricated cavity patterns and incubated at 23 °C for 2 h in a humid petri dish wetted Kimwipes (Kimtech) to reduce evaporation, with 300 rpm shaking on a BioShake iQ shaker. The chip was then transferred into a well filled with 0.9 mL 40 mM $MgCl_2$ buffer (containing 10 mM Tris and 40 mM $MgCl_2$, pH = 8.0 ± 0.2) on a 48-well culture plate (10861-560, VWR), with the patterned side up. The chip was washed by shaking the plate at 700 rpm for 5 min and then transferred into another well with 0.9 mL fresh buffer for the next wash In total, the chip was washed 4 times in 0.9 mL 40 mM $MgCl_2$ buffer and 2 times in 0.9 mL 60 mM $MgCl_2$ buffer (containing 10 mM Tris and 60 mM $MgCl_2$, pH = 9.0 ± 0.2) to remove excess DNA while enhancing substrate binding with higher Mg^{2+} concentration and higher buffer pH. The chip was then dried by quickly dipping into water twice to remove bulk residual buffer and blow-drying with pressurized air. For PMMA lift-off, the dried chip was ultrasonicated in an *N*-methylpyrrolidone

bath at Power 0 for 6 min using a sweepSONIK (40 kHz dualSWEEP) ultrasonic generator (Blackstone-NEY Ultrasonics, Cleaning Technologies Group, LLC). The chip was then immersed and stirred for 30 s in an acetone bath and IPA bath consecutively and dried with pressurized N_2.

For CSMOP on SiN_x photonic structures (1 cm × 1 cm chip), 100 µL origami solution was applied and incubated with the chip for 3 h. The chip was washed in a 24-well culture plate (10861-558, VWR) with 2 mL wash buffers each time to adapt for the larger chip size.

To silicify origami for SEM characterization (not a soft-silicification), a silicification precursor solution was prepared freshly by adding 75 µL (3-aminopropyl)triethoxysilane (APTES, 99%, 919-30-2, Sigma-Aldrich) and 150 µL tetraethyl orthosilicate (TEOS, ≥ 99% GC, 78-10-4, Sigma-Aldrich) to 4.775 mL 12.5 mM $MgCl_2$ buffer sequentially with vortex mixing in between. The mixture was incubated at room temperature with 900 rpm shaking for 30 min and left undisturbed for 20 min, followed by filtration through a 0.22 µm centrifuge tube filter (Corning Costar Spin-X). After CSMOP, prior to drying, the origami-placed chip was transferred to a new well containing 1 mL as prepared silicification precursor, and incubated for 1.5 h with 500 rpm shaking. The chip was then washed in 0.9 mL 12.5 mM $MgCl_2$ buffer 4 times in the plate wells. Drying and lift-off were the same as described above.

CSMOP directed gold NP arrangement

DNA origami with binding overhangs was first placed through CSMOP as described above until completion of 40 mM $MgCl_2$ buffer washes. The chip was removed from the buffer and its back side dried with a Kimwipe, without removing the liquid on the top side of the chip. The chip was placed back into the humid petri dish and 20 µL 10 nM DNA functionalized AuNSs (or 1 nM DNA functionalized AuNRs) in 40 mM $MgCl_2$ buffer was added onto the the chip. After pipetting the liquid in and out 10 times for mixing, the chip was incubated at room temperature for 4 h (2.5 h for AuNR). The chip was then washed 4 times in 0.9 mL 40 mM $MgCl_2$ buffer and 2 times in 0.9 mL 60 mM $MgCl_2$ buffer in the plate, followed by drying and lift-off as described above.

CSMOP directed QR arrangement

DNA origami with binding overhangs was first placed through CSMOP and then soft-silicified to accommodate Mg^{2+}-free conditions. Soft-silicification precursor solution was prepared freshly by sequentially adding 150 µL N-trimethoxysilylpropyl-N,N,N-trimethylammonium chloride (TMAPS, 50% in methanol, 35141-36-7, Fisher Scientific) and 150 µL TEOS, to 4.7 mL 12.5 mM $MgCl_2$ buffer with vortex mixing in between. This mixture was incubated at room temperature with 900 rpm shaking for 30 min and left undisturbed for 20 min to allow large silica particles to float to the top of the solution. 1 mL solution was taken from the bottom of the mixture and added to a well on the 48-well plate. After origami placement in CSMOP, the chip was washed 3 times in 0.9 mL 40 mM $MgCl_2$ buffer and once in 0.9 mL 60 mM $MgCl_2$ buffer in the plate, before transferring to the well containing the soft-silicification precursor and incubated for 1.5 h. The chip was then washed 4 times with 0.9 mL 12.5 mM $MgCl_2$ buffer and transferred to another well containing 1 mL passivation solution, which was freshly prepared by mixing 200 µL carboxyethylsilanetriol disodium salt (CTES, 25% in water, 18191-40-7, Oakwood) with 4.8 mL 12.5 mM $MgCl_2$ buffer and 30 µL concentrated hydrochloric acid (37%, 7647-01-0, Sigma-Aldrich) and filtering through an Amicon Ultra Centrifugal Filter (10 kDa, Sigma). After 15 min

incubation, the chip was washed 2 times in 0.9 mL 12.5 mM $MgCl_2$ buffer and 3 times in 0.9 mL PBS buffer (without calcium and magnesium, pH = 7.4 ± 0.1, 21-040, Corning).

The chip was removed from the buffer solution and its back side dried with a Kimwipe, without removing the liquid on the top side of the chip. The chip was placed back into the humid petri dish and 20 µL 20 nM DNA functionalized QRs in PBS buffer was added onto the chip. After pipetting the liquid in and out 10 times for mixing, the chip was incubated at room temperature for 4 h. The chip was then washed 4 times in 0.9 mL PBS buffer and 2 times in 0.9 mL 60 mM $MgCl_2$ buffer in the plate, followed by drying and lift-off as described above.

For QR placement on SiN_x photonic structure chips (1 cm × 1 cm), all steps were performed in a 24-well culture plate (10861-558, VWR) with 2 mL corresponding solutions to adjust for the larger chip size. 100 µL QR solution was used for QR binding.

Kinetic simulation

Two-dimensional projected DNA structures and corresponding deposition shapes were modeled with their nanoscale dimensions: 125 nm × 75 nm (rhombic structure), 140 nm × 40 nm (ladder-shaped structure), and 140 nm × 120 nm (triangular structure). Thermodynamic energy landscapes were calculated by establishing a conformational grid on x, y coordinates and angle θ (structure rotation relative to deposition shape). Using each deposition location as the origin, grid points were defined as: $-80\text{ nm} \leq X, Y \leq 80\text{ nm}$ with 5 nm intervals, and $-90° \leq \theta \leq 87°$ for rhombic and ladder-shaped structures and $-60° \leq \theta \leq 57°$ for triangular structure with 3° intervals. For each grid point, we calculated the overlapped area (A_o) between a structure and its deposition shape by generating alpha shapes and summing triangulated overlapped regions. The binding free energy for both non-cavity and cavity cases was determined as $E_b = u_b A_o$, where u_b is the assumed binding free energy per area (−0.001). The free energy penalty, calculated only for the cavity case, was set as $E_r = u_r A_r$, where u_r is the assumed free energy penalty per area (0.001α, with α as the free energy penalty coefficient) and A_r represents area outside the cavity. Total interaction free energy was computed as $E = E_b + E_r$.

In kinetic simulations, each grid point served as an initial conformation with DNA structures allowed to move toward energetically favorable conformations. The perturbing intervals for searching neighboring conformations were set to ± 5 nm for X and Y positions, and ± 3° for rotation angle θ. From each initial state, structures were translated or rotated to the neighboring conformation with the lowest E of its 6 neighbors until reaching a local minimum. For CSMOP simulations, initial conformations with a positive E were eliminated due to the lack of origami interaction with the cavity base (See **Supplementary Note 3-4**).

AFM and SEM characterization

AFM measurements were performed under air conditions using an Asylum Research Jupiter XR AFM (Oxford Instrument) in tapping mode with 55AC-NG gold-coated ultra-high frequency AFM probes (tip radius < 7 nm, f_o = 1200 kHz; 85 N/m, NanoAndMore). SEM imaging were conducted on a Zeiss Sigma HD VP Scanning Electron Microscope at 2 kV, using an Inlens Secondary Electron Detector for silicified CSMOP origami arrays (without coating) and an Everhart Thornley Secondary Electron Detector for SiN_x photonic structures (after 5-second gold coating with a PELCO SC-7 Sputter Coater).

Optical microscopy

Dark field microscopy of CSMOP-directed AuNR arrays utilized a Nikon Eclipse LV150NA microscope equipped with a DS-Ri2 camera and 100× air objective (Nikon MUE61900 EPI, NA 0.8), employing a rotatable polarizer for incident light and an analyzer with vertical polarization.

Confocal fluorescence imaging of QR arrays was conducted on a home-built setup using a Zeiss Eclipse TI microscope body with piezo-controlled 3D movable stage and 100× air objective (Nikon MUE42900, NA 0.9). Arrays were raster-scanned using a piezoelectric stage under 488 nm laser excitation with circularly polarized light achieved using a wire grid polarizer (ThorLabs WP25M-VIS) and a quarter waveplate (ThorLabs AQWP05M-600). Emission was filtered through a 506 nm single-edge dichroic (Semrock FF506-Di03) and 500 nm long pass filter (ThorLabs FELH0500), followed by a rotatable wire grid polarizer (ThorLabs WP25M-VIS) rotated in 20-degree increments between scans. The filtered emission was directed through a telescopic 1:1 pinhole system (20 cm lenses, 50 µm pinhole) and collected on a silicon avalanche photodiode with a time-correlated single photon counting system (Picoquant Hydraharp). Widefield PL imaging was conducted on a previously reported home-built microscope setup[112] at room temperature. A lens focused on the back focal plane of the sample was used to convert a 532 nm laser into widefield illumination. Images were collected by an electron-multiplying charge-coupled device (EMCCD) camera (Andor) with a 600 nm longpass filter.

Data processing

Detailed image processing methods to acquire sizes, yields and distributions are described in **Supplementary Note 7**.

Data availability

The data that support the findings of this study and the simulation code are openly available in the Supplementary Information files and on the open-source data repository *Dryad* at DOI: 10.5061/dryad.qrfj6q5s9.

Acknowledgements

M.B., X.L. and C.C. are grateful for funding from the U.S. Office of Naval Research (N00014-21-1-4013) and the U.S. National Science Foundation (CCF 1956054); R.J.M., X.L. and N.S. thank the U.S. Air Force Office of Scientific Research's Natural Materials and Systems Program (FA9550-23-1-0210) for funding. J.H. and L.R. are grateful for funding from the U.S. National Science Foundation ITE Convergence Accelerator Track I (ITE-2236093). M.G.B., T.S. and A.J. thank the U.S. Department of Energy for funding (DE-SC0021650). T.S. thanks the Natural Sciences and Engineering Research Council of Canada for a Postgraduate Scholarship (PGSD). J.Y.L thanks the National Research Foundation of Korea for a Sejong Science Fellowship (NRF-2021R1C1C2003554). This work was performed in part through the use of the facilities of MIT.nano and the Harvard University Center for Nanoscale Systems (CNS). The authors thank Prof. Dirk Englund and Isaac B.W. Harris for access to the widefield fluorescence microscope.

Author contributions

M.B., R.J.M. and X.L. conceived the research and drafted the manuscript. X.L. developed the methods of CSMOP and the integration of NPs and QRs on patterned silicon chips. X.L. performed and optimized DNA origami design and assembly, materials synthesis, resist cavity fabrication, nanomaterials placement, dark-field microscopy, and AFM characterization. L.R. and J.H. designed and fabricated chips with silicon nitride photonic structures. T.S., A.J. and M.G.B. designed and conducted fluorescence and emission polarization experiments. J.Y.L. developed the computational code and performed kinetic simulations. N.S. conducted SEM characterization. C.C. optimized QR-DNA synthesis. All authors contributed to manuscript writing and revision.

Competing interests

M.B., R.J.M., C.C. and X.L. are co-inventors on a patent application (WO2024186458A2) including the CSMOP method. The patent application (PCT/US2024/016144) was filed by Massachusetts Institute of Technology on Feb. 16, 2024. The authors declare no other competing interests.

References

1. Elshaari, A.W., Pernice, W., Srinivasan, K., Benson, O. & Zwiller, V. Hybrid integrated quantum photonic circuits. *Nat. Photonics* **14**, 285–298 (2020).
2. Shekhar, S. et al. Roadmapping the next generation of silicon photonics. *Nat. Commun.* **15**, 751 (2024).
3. Pelucchi, E. et al. The potential and global outlook of integrated photonics for quantum technologies. *Nat. Rev. Phys.* **4**, 194-208 (2022).
4. Redjem, W. et al. All-silicon quantum light source by embedding an atomic emissive center in a nanophotonic cavity. *Nat. Commun.* **14**, 3321 (2023).
5. Hollenbach, M. et al. Wafer-scale nanofabrication of telecom single-photon emitters in silicon. *Nat. Commun.* **13**, 7683 (2022).
6. Somaschi, N. et al. Near-optimal single-photon sources in the solid state. *Nat. Photonics* **10**, 340-345 (2016).
7. Uppu, R. et al. Scalable integrated single-photon source. *Sci. Adv.* **6**, eabc8268 (2020).
8. Aharonovich, I. & Prawer, S. Fabrication strategies for diamond based ultra bright single photon sources. *Diamond Relat. Mater.* **19**, 729-733 (2010).
9. Agarwal, K., Rai, H. & Mondal, S. Quantum dots: an overview of synthesis, properties, and applications. *Mater. Res. Express* **10**, 062001 (2023).
10. Gaita-Ariño, A., Luis, F., Hill, S. & Coronado, E. Molecular spins for quantum computation. *Nat. Chem.* **11**, 301-309 (2019).
11. Wasielewski, M.R. et al. Exploiting chemistry and molecular systems for quantum information science. *Nat. Rev. Chem.* **4**, 490-504 (2020).
12. Murray, C.B., Norris, D.J. & Bawendi, M.G. Synthesis and characterization of nearly monodisperse CdE (E = sulfur, selenium, tellurium) semiconductor nanocrystallites. *J. Am. Chem. Soc.* **115**, 8706-8715 (1993).
13. Zhu, H. et al. Synthesis of Zwitterionic CsPbBr3 Nanocrystals with Controlled Anisotropy using Surface-Selective Ligand Pairs. *Adv. Mater.* **35**, 2304069 (2023).

14. Zhao, S. et al. Single photon emission from graphene quantum dots at room temperature. *Nat. Commun.* **9**, 3470 (2018).
15. Almutlaq, J. et al. Engineering colloidal semiconductor nanocrystals for quantum information processing. *Nat. Nanotechnol.* **19**, 1091–1100 (2024).
16. Kloeffel, C. & Loss, D. Prospects for spin-based quantum computing in quantum dots. *Annu. Rev. Condens. Matter Phys.* **4**, 51-81 (2013).
17. Ye, Y., Lin, X. & Fang, W. Room-Temperature Single-Photon Sources Based on Colloidal Quantum Dots: A Review. *Materials* **16**, 7684 (2023).
18. Elsinger, L. et al. Integration of Colloidal PbS/CdS Quantum Dots with Plasmonic Antennas and Superconducting Detectors on a Silicon Nitride Photonic Platform. *Nano Lett.* **19**, 5452-5458 (2019).
19. Wang, X.-D. et al. Waveguide-coupled deterministic quantum light sources and post-growth engineering methods for integrated quantum photonics. *Chip* **1**, 100018 (2022).
20. Dhawan, A.R., Nasilowski, M., Wang, Z., Dubertret, B. & Maitre, A. Fabrication of Efficient Single-Emitter Plasmonic Patch Antennas by Deterministic In Situ Optical Lithography using Spatially Modulated Light. *Adv. Mater.* **34**, e2108120 (2022).
21. Sapienza, L., Davanco, M., Badolato, A. & Srinivasan, K. Nanoscale optical positioning of single quantum dots for bright and pure single-photon emission. *Nat. Commun.* **6**, 7833 (2015).
22. Liu, X. et al. On-chip generation of single-photon circularly polarized single-mode vortex beams. *Sci. Adv.* **9**, eadh0725 (2023).
23. Weng, H.C. et al. Heterogeneous Integration of Solid-State Quantum Systems with a Foundry Photonics Platform. *ACS Photonics* **10**, 3302-3309 (2023).
24. Eich, A. et al. Single-Photon Emission from Individual Nanophotonic-Integrated Colloidal Quantum Dots. *ACS Photonics* **9**, 551-558 (2022).
25. Xing, X. et al. High-resolution combinatorial patterning of functional nanoparticles. *Nat. Commun.* **11**, 6002 (2020).
26. Jiang, M., Kurvits, J.A., Lu, Y., Nurmikko, A.V. & Zia, R. Reusable Inorganic Templates for Electrostatic Self-Assembly of Individual Quantum Dots, Nanodiamonds, and Lanthanide-Doped Nanoparticles. *Nano Lett.* **15**, 5010-5016 (2015).
27. Xie, W. et al. Nanoscale and Single-Dot Patterning of Colloidal Quantum Dots. *Nano Lett.* **15**, 7481-7487 (2015).
28. Zhang, Q. et al. Large ordered arrays of single photon sources based on II–VI semiconductor colloidal quantum dot. *Opt. Express* **16**, 19592-19599 (2008).
29. Barelli, M. et al. Single-Photon Emitting Arrays by Capillary Assembly of Colloidal Semiconductor CdSe/CdS/SiO_2 Nanocrystals. *ACS Photonics* **10**, 1662-1670 (2023).
30. Nguyen, H.A. et al. Deterministic Quantum Light Arrays from Giant Silica-Shelled Quantum Dots. *ACS Appl. Mater. Interfaces* **15**, 4294-4302 (2023).
31. Cheng, G. et al. Single CdSe Quantum Dots Positioned in Nanostructured Heterogeneous Templates: Implications for High-Precision Nanoassembly. *ACS Appl. Nano Mater.* **5**, 5756-5763 (2022).
32. Meng, Y. et al. Deterministic Assembly of Single Sub‐20 nm Functional Nanoparticles Using a Thermally Modified Template with a Scanning Nanoprobe. *Adv. Mater.* **32**, 2005979 (2020).
33. Ni, S., Leemann, J., Buttinoni, I., Isa, L. & Wolf, H. Programmable colloidal molecules from sequential capillarity-assisted particle assembly. *Sci. Adv.* **2**, e1501779 (2016).

34. Flauraud, V. et al. Nanoscale topographical control of capillary assembly of nanoparticles. *Nat. Nanotechnol.* **12**, 73-80 (2017).
35. Funke, J.J. & Dietz, H. Placing molecules with Bohr radius resolution using DNA origami. *Nat. Nanotechnol.* **11**, 47-52 (2016).
36. Adamczyk, A.K. et al. DNA Self-Assembly of Single Molecules with Deterministic Position and Orientation. *ACS Nano* **16**, 16924-16931 (2022).
37. Gorman, J. et al. Sculpting photoproducts with DNA origami. *Chem* (2024).
38. Liu, N. & Liedl, T. DNA-assembled advanced plasmonic architectures. *Chem. Rev.* **118**, 3032-3053 (2018).
39. Hartl, C. et al. Position Accuracy of Gold Nanoparticles on DNA Origami Structures Studied with Small-Angle X-ray Scattering. *Nano Lett.* **18**, 2609-2615 (2018).
40. Glembockyte, V., Grabenhorst, L., Trofymchuk, K. & Tinnefeld, P. DNA Origami Nanoantennas for Fluorescence Enhancement. *Acc. Chem. Res.* **54**, 3338-3348 (2021).
41. Ge, H. et al. Sequence-Dependent DNA Functionalization of Upconversion Nanoparticles and Their Programmable Assemblies. *Angew. Chem. Int. Ed.* **59**, 8133-8137 (2020).
42. Chen, C. et al. Nanoscale 3D spatial addressing and valence control of quantum dots using wireframe DNA origami. *Nat. Commun.* **13**, 4935 (2022).
43. Chen, C. et al. Ultrafast dense DNA functionalization of quantum dots and rods for scalable 2D array fabrication with nanoscale precision. *Sci. Adv.* **9**, eadh8508 (2023).
44. Huang, D., Haddad, L., Rahman, F., Palma, M. & Sapelkin, A. Engineering a DNA origami mediated multicolour quantum dot platform for sub-diffraction spectral separation imaging. *RSC Advances* **12**, 23778-23785 (2022).
45. Ko, S.H., Du, K. & Liddle, J.A. Quantum-dot fluorescence lifetime engineering with DNA origami constructs. *Angew. Chem. Int. Ed. Engl.* **52**, 1193-1197 (2013).
46. Bui, H. et al. Programmable periodicity of quantum dot arrays with DNA origami nanotubes. *Nano Lett.* **10**, 3367-3372 (2010).
47. Gür, F.N. et al. DNA-Assembled Plasmonic Waveguides for Nanoscale Light Propagation to a Fluorescent Nanodiamond. *Nano Lett.* **18**, 7323-7329 (2018).
48. Zhang, T. et al. DNA-Based Self-Assembly of Fluorescent Nanodiamonds. *J. Am. Chem. Soc.* **137**, 9776-9779 (2015).
49. Kershner, R.J. et al. Placement and orientation of individual DNA shapes on lithographically patterned surfaces. *Nat. Nanotechnol.* **4**, 557-561 (2009).
50. Gopinath, A. & Rothemund, P.W.K. Optimized Assembly and Covalent Coupling of Single-Molecule DNA Origami Nanoarrays. *ACS Nano* **8**, 12030-12040 (2014).
51. Gopinath, A., Miyazono, E., Faraon, A. & Rothemund, P.W.K. Engineering and mapping nanocavity emission via precision placement of DNA origami. *Nature* **535**, 401-405 (2016).
52. Gopinath, A. et al. Absolute and arbitrary orientation of single-molecule shapes. *Science* **371**, eabd6179 (2021).
53. Martynenko, I.V. et al. Site-directed placement of three-dimensional DNA origami. *Nat. Nanotechnol.* **18**, 1456-1462 (2023).
54. Sikeler, C., Haslinger, F., Martynenko, I.V. & Liedl, T. DNA Origami-Directed Self-Assembly of Gold Nanospheres for Plasmonic Metasurfaces. *Adv. Funct. Mater.* **34**, 2404766 (2024).
55. Huang, D., Freeley, M. & Palma, M. DNA-Mediated Patterning of Single Quantum Dot Nanoarrays: A Reusable Platform for Single-Molecule Control. *Sci. Rep.* **7**, 45591 (2017).

56. Scheible, M.B., Pardatscher, G., Kuzyk, A. & Simmel, F.C. Single Molecule Characterization of DNA Binding and Strand Displacement Reactions on Lithographic DNA Origami Microarrays. *Nano Lett.* **14**, 1627-1633 (2014).
57. Gerdon, A.E. et al. Controlled Delivery of DNA Origami on Patterned Surfaces. *Small* **5**, 1942-1946 (2009).
58. Penzo, E., Wang, R., Palma, M. & Wind, S.J. Selective placement of DNA origami on substrates patterned by nanoimprint lithography. *J. Vac. Sci. Technol. B* **29**, 06F205 (2011).
59. Brassat, K. et al. On the Adsorption of DNA Origami Nanostructures in Nanohole Arrays. *Langmuir* **34**, 14757-14765 (2018).
60. Shetty, R.M., Brady, S.R., Rothemund, P.W.K., Hariadi, R.F. & Gopinath, A. Bench-Top Fabrication of Single-Molecule Nanoarrays by DNA Origami Placement. *ACS Nano* **15**, 11441-11450 (2021).
61. Pirandola, S., Bardhan, B.R., Gehring, T., Weedbrook, C. & Lloyd, S. Advances in photonic quantum sensing. *Nat. Photonics* **12**, 724-733 (2018).
62. Zhong, H.-S. et al. Quantum computational advantage using photons. *Science* **370**, 1460-1463 (2020).
63. Luo, W. et al. Recent progress in quantum photonic chips for quantum communication and internet. *Light Sci. Appl.* **12**, 175 (2023).
64. Zhou, Y. et al. Shape-Selective Deposition and Assembly of Anisotropic Nanoparticles. *Nano Lett.* **14**, 2157-2161 (2014).
65. Zhou, W. et al. Device-quality, reconfigurable metamaterials from shape-directed nanocrystal assembly. *Proc. Natl. Acad. Sci. U.S.A.* **117**, 21052-21057 (2020).
66. Jun, H., Wang, X., Bricker, W.P. & Bathe, M. Automated sequence design of 2D wireframe DNA origami with honeycomb edges. *Nat. Commun.* **10**, 5419 (2019).
67. Wang, X. et al. Planar 2D wireframe DNA origami. *Sci. Adv.* **8**, eabn0039 (2022).
68. Wagenbauer, K.F. et al. How We Make DNA Origami. *ChemBioChem* **18**, 1873-1885 (2017).
69. Shaw, A., Benson, E. & Högberg, B. Purification of Functionalized DNA Origami Nanostructures. *ACS Nano* **9**, 4968-4975 (2015).
70. Tapio, K. et al. Large-Scale Formation of DNA Origami Lattices on Silicon. *Chem. Mater.* **35**, 1961-1971 (2023).
71. Woo, S. & Rothemund, P.W.K. Self-assembly of two-dimensional DNA origami lattices using cation-controlled surface diffusion. *Nat. Commun.* **5**, 4889 (2014).
72. Xin, Y., Martinez Rivadeneira, S., Grundmeier, G., Castro, M. & Keller, A. Self-assembly of highly ordered DNA origami lattices at solid-liquid interfaces by controlling cation binding and exchange. *Nano Res.* **13**, 3142-3150 (2020).
73. Lin, Q.-Y. et al. Building superlattices from individual nanoparticles via template-confined DNA-mediated assembly. *Science* **359**, 669-672 (2018).
74. Hung, A.M. et al. Large-area spatially ordered arrays of gold nanoparticles directed by lithographically confined DNA origami. *Nat. Nanotechnol.* **5**, 121-126 (2010).
75. Zheng, J. et al. Gold Nanorods: The Most Versatile Plasmonic Nanoparticles. *Chem. Rev.* **121**, 13342-13453 (2021).
76. Kuemin, C., Nowack, L., Bozano, L., Spencer, N.D. & Wolf, H. Oriented Assembly of Gold Nanorods on the Single‐Particle Level. *Adv. Funct. Mater.* **22**, 702-708 (2011).

77. Huang, Y. & Kim, D.H. Dark-field microscopy studies of polarization-dependent plasmonic resonance of single gold nanorods: rainbow nanoparticles. *Nanoscale* **3**, 3228-3232 (2011).
78. Zhang, H. et al. Direct Assembly of Large Area Nanoparticle Arrays. *ACS Nano* **12**, 7529-7537 (2018).
79. Li, Z., Liu, W., Cheng, H., Chen, S. & Tian, J. Manipulation of the Photonic Spin Hall Effect with High Efficiency in Gold-Nanorod-Based Metasurfaces. *Adv. Opt. Mater.* **5**, 1700413 (2017).
80. Cai, J., Zhang, C. & Li, W.-D. Dual-Color Flexible Metasurfaces with Polarization-Tunable Plasmons in Gold Nanorod Arrays. *Adv. Opt. Mater.* **9**, 2001401 (2021).
81. Zijlstra, P., Chon, J.W.M. & Gu, M. Five-dimensional optical recording mediated by surface plasmons in gold nanorods. *Nature* **459**, 410-413 (2009).
82. Taylor, A.B., Michaux, P., Mohsin, A.S.M. & Chon, J.W.M. Electron-beam lithography of plasmonic nanorod arrays for multilayered optical storage. *Opt. Express* **22**, 13234-13243 (2014).
83. Liu, M. et al. Colloidal quantum dot electronics. *Nat. Electron.* **4**, 548-558 (2021).
84. Shirasaki, Y., Supran, G.J., Bawendi, M.G. & Bulović, V. Emergence of colloidal quantum-dot light-emitting technologies. *Nat. Photonics* **7**, 13-23 (2012).
85. Kagan, C.R., Bassett, L.C., Murray, C.B. & Thompson, S.M. Colloidal Quantum Dots as Platforms for Quantum Information Science. *Chem. Rev.* **121**, 3186-3233 (2021).
86. Li, L.-s., Hu, J., Yang, W. & Alivisatos, A.P. Band Gap Variation of Size- and Shape-Controlled Colloidal CdSe Quantum Rods. *Nano Lett.* **1**, 349-351 (2001).
87. Srivastava, A.K., Zhang, W., Schneider, J., Halpert, J.E. & Rogach, A.L. Luminescent Down-Conversion Semiconductor Quantum Dots and Aligned Quantum Rods for Liquid Crystal Displays. *Adv. Sci.* **6**, 1901345 (2019).
88. Zhang, Q. et al. Perovskite Light‐Emitting Diodes with Quantum Wires and Nanorods. *Adv. Mater.*, 2405418 (2024).
89. Pisanello, F. et al. Dots in rods as polarized single photon sources. *Superlattices Microstruct.* **47**, 165-169 (2010).
90. Jing, X. et al. Solidifying framework nucleic acids with silica. *Nat. Protoc.* **14**, 2416-2436 (2019).
91. Liu, X. et al. Complex silica composite nanomaterials templated with DNA origami. *Nature* **559**, 593-598 (2018).
92. Wassermann, L.M., Scheckenbach, M., Baptist, A.V., Glembockyte, V. & Heuer-Jungemann, A. Full Site-Specific Addressability in DNA Origami-Templated Silica Nanostructures. *Adv. Mater.* **35**, 2212024 (2023).
93. Yuan, G., Gomez, D.E., Kirkwood, N., Boldt, K. & Mulvaney, P. Two Mechanisms Determine Quantum Dot Blinking. *ACS Nano* **12**, 3397-3405 (2018).
94. Galland, C. et al. Two types of luminescence blinking revealed by spectroelectrochemistry of single quantum dots. *Nature* **479**, 203-207 (2011).
95. Mahler, B. et al. Towards non-blinking colloidal quantum dots. *Nat. Mater.* **7**, 659-664 (2008).
96. Chen, O. et al. Compact high-quality CdSe-CdS core-shell nanocrystals with narrow emission linewidths and suppressed blinking. *Nat. Mater.* **12**, 445-451 (2013).
97. Shi, J. et al. All-optical fluorescence blinking control in quantum dots with ultrafast mid-infrared pulses. *Nat. Nanotechnol.* **16**, 1355-1361 (2021).

98. le Feber, B., Prins, F., De Leo, E., Rabouw, F.T. & Norris, D.J. Colloidal-Quantum-Dot Ring Lasers with Active Color Control. *Nano Lett.* **18**, 1028-1034 (2018).
99. Weeber, J.-C. et al. Colloidal quantum dots decorated micro-ring resonators for efficient integrated waveguides excitation. *Nanophotonics* **9**, 1411-1423 (2020).
100. Ma, J. et al. Engineering Quantum Light Sources with Flat Optics. *Adv. Mater.* **36**, 2313589 (2024).
101. Peniakov, G. et al. Polarized and Unpolarized Emission from a Single Emitter in a Bullseye Resonator. *Laser Photonics Rev.* **18**, 2300835 (2024).
102. Zhang, X. et al. Adsorption of DNA Oligonucleotides by Titanium Dioxide Nanoparticles. *Langmuir* **30**, 839-845 (2014).
103. Kaminska, I. et al. Distance Dependence of Single-Molecule Energy Transfer to Graphene Measured with DNA Origami Nanopositioners. *Nano Lett.* **19**, 4257-4262 (2019).
104. Jin, Z. et al. Metallized DNA nanolithography for encoding and transferring spatial information for graphene patterning. *Nat. Commun.* **4**, 1663 (2013).
105. Park, H.-Y. et al. n- and p-Type Doping Phenomenon by Artificial DNA and M-DNA on Two-Dimensional Transition Metal Dichalcogenides. *ACS Nano* **8**, 11603-11613 (2014).
106. Wang, J., Sciarrino, F., Laing, A. & Thompson, M.G. Integrated photonic quantum technologies. *Nat. Photonics* **14**, 273-284 (2020).
107. Jun, H. et al. Rapid prototyping of arbitrary 2D and 3D wireframe DNA origami. *Nucleic Acids Res.* **49**, 10265-10274 (2021).
108. Wang, X., Jun, H. & Bathe, M. Programming 2D Supramolecular Assemblies with Wireframe DNA Origami. *J. Am. Chem. Soc.* **144**, 4403–4409 (2022).
109. Liu, B. & Liu, J. Freezing Directed Construction of Bio/Nano Interfaces: Reagentless Conjugation, Denser Spherical Nucleic Acids, and Better Nanoflares. *J. Am. Chem. Soc.* **139**, 9471-9474 (2017).
110. Bastús, N.G., Comenge, J. & Puntes, V. Kinetically Controlled Seeded Growth Synthesis of Citrate-Stabilized Gold Nanoparticles of up to 200 nm: Size Focusing versus Ostwald Ripening. *Langmuir* **27**, 11098-11105 (2011).
111. Hao, Y., Li, Y., Song, L. & Deng, Z. Flash Synthesis of Spherical Nucleic Acids with Record DNA Density. *J. Am. Chem. Soc.* **143**, 3065-3069 (2021).
112. Harris, I.B.W. et al. Hyperfine Spectroscopy of Isotopically Engineered Group-IV Color Centers in Diamond. *PRX Quantum* **4**, 040301 (2023).